Validating density-functional theory simulations at high energy-density conditions with liquid krypton shock experiments to 850 GPa on Sandia's Z machine

Thomas R. Mattsson,[*] Seth Root,[†] Ann E. Mattsson,[‡] Luke Shulenburger,[§] Rudolph J. Magyar,[‖] and Dawn G. Flicker[¶]
Sandia National Laboratories, Albuquerque, New Mexico 87185, USA

(Received 1 July 2014; revised manuscript received 30 September 2014; published 11 November 2014)

We use Sandia's Z machine and magnetically accelerated flyer plates to shock compress liquid krypton to 850 GPa and compare with results from density-functional theory (DFT) based simulations using the AM05 functional. We also employ quantum Monte Carlo calculations to motivate the choice of AM05. We conclude that the DFT results are sensitive to the quality of the pseudopotential in terms of scattering properties at high energy/temperature. A new Kr projector augmented wave potential was constructed with improved scattering properties which resulted in excellent agreement with the experimental results to 850 GPa and temperatures above 10 eV (110 kK). Finally, we present comparisons of our data from the Z experiments and DFT calculations to current equation of state models of krypton to determine the best model for high energy-density applications.

DOI: 10.1103/PhysRevB.90.184105 PACS number(s): 62.50.Ef, 71.15.Pd, 82.35.Lr

I. INTRODUCTION

Density-functional theory (DFT) [1] has emerged as the method of choice for first-principles simulations of material's properties under high energy-density conditions, for example, the extreme pressures and temperatures reached under shock compression. There are now many examples of accurate DFT simulations compared to high-precision experimental data, primarily from first- and second-row elements and compounds such as hydrogen [2], carbon [3], quartz [4], water [5], and carbon dioxide [6]. Part of the reason that DFT has been so successful in this role is its ability to account for the effects of high temperatures and pressures due to the use of the Mermin formulation [7]. The inability of classical potentials to accurately reproduce very wide range Hugoniots can be directly attributable to this inability to explicitly model the changing degrees of freedom that different temperatures imply [8].

Although DFT is a formally exact reformulation of the quantum mechanical many-body problem, providing a path to observables via density functionals, different types of approximations enter during the course of performing large-scale quantum molecular dynamics (QMD) simulations. Considerable interest exists in validating calculations for elements with higher atomic number in regimes of high density, temperature, and pressure. The properties of krypton make it ideal to study these effects on heavier elements; the initial state of cryogenically cooled liquid krypton is well known. Extensive literature on static compression of krypton at low temperatures that provides a valuable reference on how pressure affects the solid phase and its melting behavior [9–13]. Upon shock compression, krypton turns metallic, resulting in a reflective shock front, allowing for very high-precision measurements of the shock velocity. Few experimental data on krypton at high pressures exist, with prior Hugoniot data limited to just below 100 GPa. Obtaining data in the range of several hundreds of GPa would provide knowledge of the behavior of krypton at a significantly increased range in density, temperature, and pressure.

In addition to the broad experimental motivation for this work, our initial DFT krypton Hugoniot calculations indicated that the standard projector augmented wave (PAW) potential distributed with VASP was inadequate at the high pressures and temperatures occurring under strong shock compression, raising important questions about verification of PAW potentials and validation of QMD as a method in general at very high temperatures. In this paper, we describe an approach to evaluating and constructing PAW potentials with high fidelity for application to high pressure, density, and temperature. We furthermore examine the liquid krypton Hugoniot to pressures of 1035 GPa using QMD and present quantum Monte Carlo (QMC) calculations on liquid krypton. Finally, we present data from shock compression experiments on Sandia's Z machine. Following the Introduction is a section on employing DFT for simulations under high energy-density (HED) conditions with emphasis on construction of high-quality PAW potentials and using QMC calculations to compare functionals, a section describing the design, diagnostics, and analysis of shock experiments on Z, and finally a section devoted to results and discussions.

II. FIRST-PRINCIPLES SIMULATIONS: DFT AND QMC

DFT [1] is a formally exact reformulation of the quantum mechanical many-body problem that results in a significant reduction in computational complexity compared to methods that rely on direct solutions of the Schrödinger equation [1]. In translating this fundamental theory into an algorithm for performing computations, approximations must be made. The approximations necessary to perform simulations of hundreds of atoms and how to systematically converge the calculations are discussed in detail in Ref. [14]. In this paper, we will discuss two aspects: the choice of exchange-correlation (XC) functional and the construction of PAW core potentials with high fidelity for use at high temperature.

[*]trmatts@sandia.gov
[†]sroot@sandia.gov
[‡]aematts@sandia.gov
[§]lshulen@sandia.gov
[‖]rjmagya@sandia.gov
[¶]dgflick@sandia.gov

A. Selecting an exchange-correlation functional

The most important fundamental approximation in any DFT calculation is the choice of an approximate XC functional. The XC functional incorporates all many-body quantum physics effects and via its functional derivative with respect to density, in turn, incorporates these into an effective potential for independent particles. We look to choose between two complementary functionals: LDA [15] and AM05 [16]. Local density approximation (LDA) is expected to perform accurately in the high-density limit where the electron distribution is close to uniform while the AM05 functional includes a dependence on the dimensionless gradient in addition to the density and is designed to capture the effects of surfaces by matching results for a surface system, the Airy gas [17]. In the high-density limit, the functional approaches LDA. AM05 has a high fidelity for several classes of solids [18,19] under normal conditions and its performance under shock compression is also excellent. For example, AM05 has been validated for shock compression of compressed SiO_2 to 1700 GPa [4]. AM05 shows a complete absence of van der Waals (vdW) attraction [19]. The result is monotonic predictable behavior for low density allowing for more straightforward inclusion of vdW, if necessary, in contrast with functionals for which a spurious interaction has to be compensated.

No *a priori* way exists for choosing which density functional will most accurately reproduce the many-body physics of a given system, be it of atomic, molecular, or condensed matter character. In the case of krypton, strong *a posteriori* clues due to prior work on the xenon Hugoniot [20] suggest that the AM05 functional [16] will perform well. However, the handling of the initial (relatively low pressure and cryogenic) state of these calculations causes some concern given that AM05 by design will not bind solid noble gases. Ideally, as we are after thermodynamic properties, we would like to choose a functional that can at least reproduce the proper dynamics of the ions under all temperatures and pressures we consider. In a canonical ensemble where the particle number, density, and temperature are held fixed (NVT), the ionic configurations should be sampled from a Boltzmann distribution. The probability of sampling any state of the system is then dependent only on the relative energies of those states. So if the functional can reproduce the relative energy ordering of different ionic configurations, this will increase confidence that the dynamics is accurate.

To test the accuracy of two density functionals for the cryogenic unshocked state of liquid krypton, we apply the explicitly many-body diffusion quantum Monte Carlo method (DMC) which is a method for solving the Schrödinger equation directly. In this computational technique, there is no effective Hamiltonian and long-range interactions are evaluated exactly, rendering it an excellent choice for the study of materials where van der Waals interactions are important [21]. In performing DMC calculations of krypton, we use the same pseudopotentials and other methodology as was recently reported in Ref. [22], which found excellent agreement with hydrostatic pressure experiments for the bulk modulus and x-ray diffraction experiments for the equilibrium lattice constant once zero point motion is considered [23,24].

To compare LDA and AM05 for liquid krypton, we extracted snapshots of the atomic positions from 32-atom

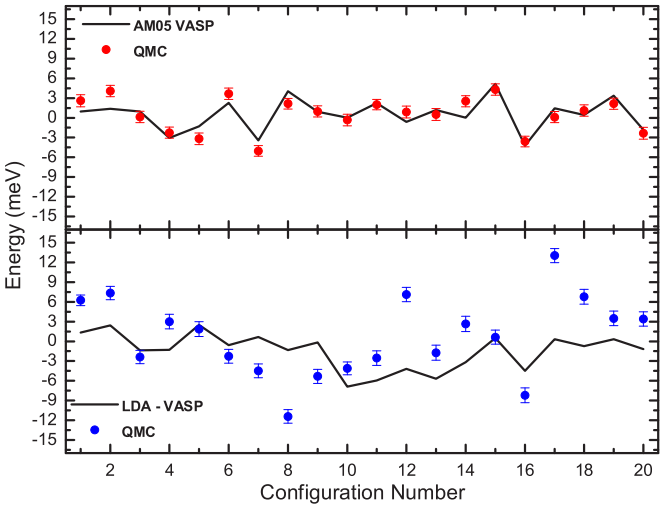

FIG. 1. (Color online) Relative energies of snapshots of 32-atom cells of Kr at 118 K and 2.43 g/cc. The top panel compares DMC energies of snapshots extracted from AM05 calculations to the AM05 energetics. The bottom panel shows the same for snapshots extracted from LDA based QMD simulations. The poor agreement is due to clumping of the liquid from negative pressure.

QMD simulations at the density (2.43 g/cc) and temperature (118 K) corresponding to the initial state of the krypton fluid used in the shock compression experiments. In each case, we compare the energies obtained using DMC as performed by the QMCPACK code [25] to those from the DFT calculations. The two functionals show a marked difference (Fig. 1), with the energies from AM05 tracking those calculated with DMC and the LDA results having an altogether different behavior. Additionally, the spread of the energies in the case of the LDA indicates that even if the ionic configurations were representative of the proper fluid, the energetics correspond to a system at a higher temperature than the 118 K desired. The reason for this behavior is that the condition of these simulations corresponds to a negative pressure state in LDA and, as a result, the atoms form clumps rather than exhibiting liquidlike behavior. These results, coupled with the results for xenon under shock compression [20], provide convincing validation for the applicability of AM05 to the krypton Hugoniot. The combination of DFT and QMC offers a general approach for improving the predictive capability of DFT simulations; a particularly important aspect for modeling materials where properties are unknown and experiments are difficult, expensive, or perhaps even impossible to perform. A similar methodology has also been used recently to assess functionals for use with dense hydrogen and water [26,27].

B. Construction and validation of PAW potentials

The second necessary approximation for performing large-scale molecular dynamics simulations that determines forces and energies from DFT calculations is the use of core potentials to remove the need to include large numbers of electrons in the calculations and to reduce the size of the plane-wave basis necessary to describe the valence. In practice, chemically inert core electrons are replaced by a pseudopotential (PP) and only

the valence electrons are treated explicitly. High-quality PPs are available for VASP [28] and other codes. It is important to distinguish the role of these potentials in an *ab initio* setting as compared to the construction of classical potentials. For *ab initio* work, the role of the pseudopotential is to integrate over irrelevant degrees of freedom (such as tightly bound core electronic states) while still reproducing the same problem for the remaining degrees of freedom. The development of PAWs for density-functional theory was an important step in this direction given that this construction provides a direct analytic mapping between the pseudized problem and the bare all-electron problem that would in principle be solved given infinite computational resources. This philosophy is in contrast to classical simulations where the role of the potential is to reproduce the physical characteristics of the system. In DFT, for instance, this is exclusively the province of the exchange-correlation functional and attempts to change the physics via the PP should be viewed with extreme caution.

With this in mind, we have very carefully worked to analyze the PAWs used for two reasons. First is that the extreme pressures and temperatures accessed on the Hugoniot of krypton are far from the conditions where pseudopotentials are normally tested. It is important to verify the accuracy of the mapping from the pseudoproblem to the all-electron one in these conditions. Second, at these extreme states, entirely different degrees of freedom may be accessed (for instance, excitations of the normally inert $3d$ electrons) and the PAWs used should allow for this flexibility in regions of phase space where this is necessary. Details of this investigation are presented in the Appendix.

C. Quantum molecular dynamics

The DFT-MD simulations were performed with VASP 5.3.3 [29] using stringent convergence settings [14,30]. Electronic states were occupied according to Mermin's finite-temperature formulation of DFT [7], which is essential for performing QMD simulations with high fidelity in the warm dense matter regime [2,14]. The simulations are performed within the NVT ensemble with velocity scaling used to enforce the ionic temperature. The shock experiments generate a Hugoniot curve, the loci of end states reached in a single shock, defined with respect to a given reference state.

The reference state for the calculations is the experimental initial conditions of liquid krypton at a density of 2.43 g/cm^3 at $T = 118$ K. The hydrostatic Hugoniot condition is expressed as $2(E - E_{\text{ref}}) = (P + P_{\text{ref}})(v_{\text{ref}} - v)$ with E the internal energy per atom, P the system pressure, and v the volume per atom. E_{ref} and P_{ref} are the energy and pressure in the initial state. The Hugoniot points were calculated by performing simulations at several temperatures for each density of interest for low and medium compression, while keeping the temperature fixed and changing the density in small increments, for the steep section of the Hugoniot where the shock pressure is not as sensitive to the temperature as it is to the density. A change from temperature to density increments significantly improves numerical convergence in the high-temperature regime. A typical fully thermalized simulation requires of the order 4000 to 8000 time steps. The velocity Verlet algorithm was used with a time step ranging from 0.5 to 4 fs depending on temperature, maintaining stable ionic trajectories requiring on the order of 3 to 10 electronic iterations per ionic step. The results from QMD simulations are shown in the Fig. 2 and Sec. IV A.

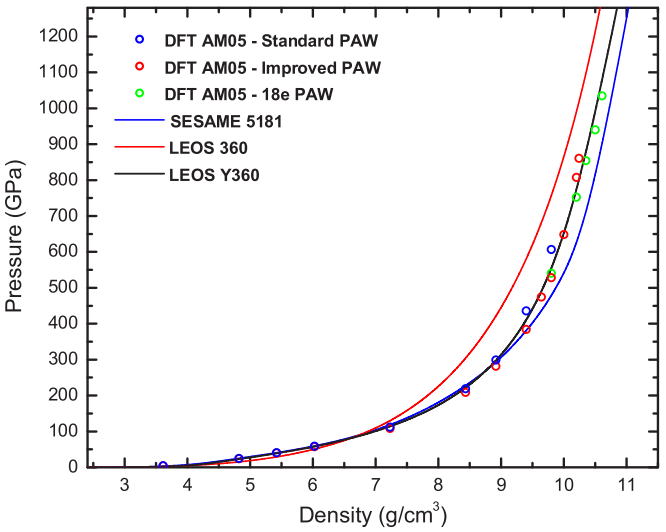

FIG. 2. (Color online) Shock Hugoniot of liquid krypton calculated with different PAW potentials using the AM05 XC functional together with tabular equation of state models.

As predicted in the Appendix, initial DFT Hugoniot calculations on krypton indicated that the standard PAW potential distributed with VASP was inadequate at high pressures and high temperatures occurring under shock compression. Figure 2 shows the standard PAW gives a significant steepening of the Hugoniot at high compression, very similar to the behavior seen for the standard xenon potential [30]. Two new krypton PAW potentials were therefore constructed, both with improved scattering properties for the atom at high energies (see Fig. 10), and a behavior in pressure that agrees with experimental data. Details of the PAW construction are found in the Appendix. Briefly, one of the new PAWs has eight electrons in the valence and is valid at a far wider range of energies than the standard PAW. The other potential has 18 electrons in the valence and is thus more suitable for the highest temperatures and pressures considered as core excitations are likely to be important in that regime. The simulation results for the principal Hugoniot are listed in Table I.

III. SHOCK EXPERIMENTS ON SANDIA'S Z MACHINE

To validate the high P-T response of liquid Kr and validate the DFT simulations, a series of shock compression experiments were performed on the Sandia Z accelerator [31]. Z is a pulsed power accelerator capable of producing currents and magnetic fields greater than 20 MA and 10 MG, respectively. The large current and field densities generate magnetic pressures up to ~650 GPa that can accelerate flyer plates up to 40 km/s [32]. The use of Z for performing shock experiments has been demonstrated for a wide range of materials and validated against traditional plate impact methods [33,34].

TABLE I. QMD calculations of the principal Hugoniot for shock compressed liquid krypton with an initial density of 2.43 g/cm^3. The points in the table are the calculated thermodynamic state of the krypton in the post shock state. The AM05 XC functional was used in all calculations. At lower pressures the improved PAW with 8 electrons in the valence was used. At higher pressures, the PAW with 18 electrons in the valence was used. The asterisk indicates calculations performed using the 18-electron PAW described in the Appendix.

Density (g/cc)	Pressure (GPa)	Temperature (K)
3.615	4.0	700
4.82	24.3	8000
5.42	39.9	13 000
6.025	57.6	17 500
7.23	108	28 600
8.917	282	48 750
9.399	384	80 000
9.64	474	94 000
9.8*	540	104 000
10.2*	752	134 000
10.35*	854	146 000
10.50*	940	157 000
10.61*	1035	170 000

A. Target design

Figure 3 shows a schematic view of the shock experiment. Targets consisted of a copper cell with a 6061-T6 aluminum buffer plate (≈250 μm) and a rear Z-cut, α-quartz top-hat 1.5-mm window (single crystals, Argus International). A copper spacer ring was placed between the rear top hat and the front buffer plate. The spacer ring and top hat set the sample thickness, which was approximately 300 μm. For one experiment, the aluminum front plate was replaced with a Z-cut, α-quartz buffer. The sample space was filled with high-purity (>99.999%) krypton gas (Matheson Tri-Gas) to 16.8 psi and cooled to 118 K using a liquid nitrogen cryosystem [35]. Mass spectroscopy of the krypton gas verified the purity and

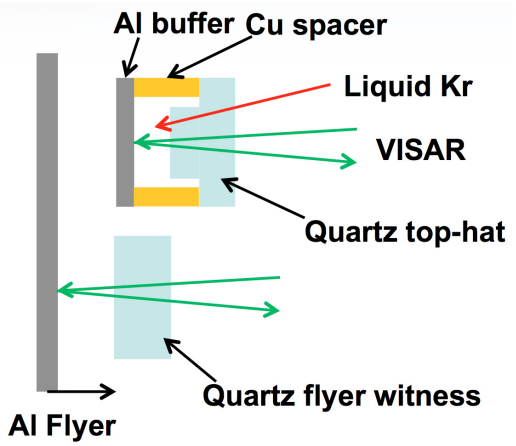

FIG. 3. (Color online) Schematic of the cryogenic call used in the Z shock compression experiments; the cell allows for long (15 ns) steady shocks (see Fig. 4).

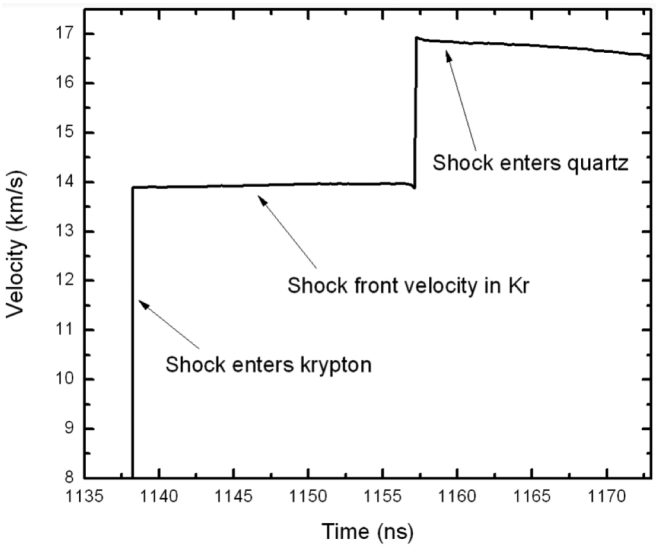

FIG. 4. Representative VISAR data. The shock transit from the aluminum drive plate into the krypton and the shock transit from the krypton to the rear quartz are indicated by sharp changes in the VISAR trace.

that the krypton was of natural isotope composition. The initial liquid krypton density was calculated from a linear fit of density-temperature data [36–39] and was 2.43 g/cc with an uncertainty of 0.5%. The refractive index of liquid krypton at 118 K was ($n = 1.30$) determined from the experimental data of Sinnock and Smith [40]. The initial density of the aluminum drive plate at 118 K was calculated using a SESAME 3700 isobar. The flyers were aluminum 6061-T6 with initial thicknesses of 1000 μm.

B. Diagnostics and analysis

A velocity interferometer system for any reflector (VISAR) [41] was used to measure flyer (V_F) and shock (U_S) velocities with an uncertainty of 0.2% to 0.5%. Multiple VISAR signals were recorded, each using different velocity per fringe settings, which eliminated 2π phase shift ambiguities upon shocks and further reduced velocity uncertainties [42]. Figure 4 shows the VISAR velocity profile from one experiment. The shock front in the krypton was reflective, so as the shock transited from the aluminum buffer plate into the krypton, the shock velocity of the krypton U_S^{Kr} was measured directly. As an independent check on the measured shock velocity, the velocity profiles were integrated to verify that the distance traveled matched the sample thickness. Directly below the krypton target was a quartz window where the aluminum flyer velocity was measured. Some tilt can exist in the target that causes the measured flyer velocity at the quartz window and at the krypton target to differ causing scatter in the experimental data. For the experiment using the quartz buffer plate, the V_F and U_S^{quartz} were measured directly.

The particle velocity, pressure, and density (U_P, P, and ρ) of the shock compressed krypton were calculated using a Monte Carlo impedance matching method (MCIM) [6,20] to solve the Rankine-Hugoniot equations [43]. A weighted

TABLE II. Experimental data for the principal Hugoniot for shock compressed liquid krypton with an initial density of 2.43 g/cm^3. The measured experimental quantities are the flyer velocity and the Kr shock velocity. For Z2294 the experimentally measured quantity is the shock velocity in the quartz buffer plate and Kr shock velocity. The asterisk indicates experiments that used a quartz drive plate. The listed velocity is the shock velocity in the quartz.

Shot	Flyer velocity (km/s)	U_P (km/s)	U_S (km/s)	ρ (g/cm^3)	Pressure (GPa)
Z2114	18.32 ± 0.06	10.21 ± 0.05	13.89 ± 0.05	9.172 ± 0.157	344.6 ± 2.1
Z2294-N*	21.05 ± 0.04*	11.51 ± 0.04	15.47 ± 0.03	9.494 ± 0.103	432.7 ± 2.0
Z2294-S*	22.96 ± 0.04*	12.50 ± 0.04	16.64 ± 0.05	9.770 ± 0.138	505.5 ± 2.4
Z2148	24.58 ± 0.06	13.43 ± 0.05	17.83 ± 0.07	9.847 ± 0.244	581.9 ± 3.1
Z2165	27.93 ± 0.07	15.11 ± 0.06	20.04 ± 0.04	9.878 ± 0.132	735.8 ± 3.6
Z2196	29.22 ± 0.09	15.78 ± 0.07	20.78 ± 0.04	10.099 ± 0.169	796.8 ± 4.3
Z2166	30.47 ± 0.09	16.46 ± 0.07	21.43 ± 0.09	10.478 ± 0.189	857.1 ± 5.0

linear fit and parameter correlation matrix for aluminum were calculated from data in Ref. [44]. The aluminum Hugoniot state prior to the shock transiting into the liquid krypton was determined using the flyer velocity measured below the target on the quartz window. In each impedance match calculation, the measured shock velocities and the initial krypton density were varied about their mean using a random number with standard deviation equal to the measurement uncertainty. Uncertainty in the aluminum Hugoniot was accounted for by varying the fit parameters about their mean using correlated random numbers. The Hugoniot state was calculated using the reflected Hugoniot of aluminum and defined as the mean of the MCIM calculation with uncertainty equal to one standard deviation. The MCIM results are corrected for the aluminum release using a release isentrope calculated from SESAME 3700. The SESAME 3700 table release was shown to have good agreement with experimentally measured deep release states for aluminum [33]. The results for the principal Hugoniot are listed in Table II. For the experiment that used α-quartz as the buffer plate, a recently developed quartz release model [45] was used in the impedance matching calculation.

The target cell geometry (Fig. 3) allowed for measurement of the reshock state in Kr. As the shock in the Kr transited into the rear quartz top hat, the shock in the quartz becomes reflective and the quartz shock velocity was measured directly. The behavior of quartz under shock compression is well characterized [4,45], which determined U_P and P states in the quartz and thus Kr accurately since U_P and P are equal at the boundary. The reshock state was calculated using the method described in Ref. [6] and the linear fit in Eq. (1). Reshock results are listed in Table III.

IV. RESULTS AND DISCUSSION

Like other low-impedance materials, the Kr Hugoniot data have been limited to pressures obtainable using gas guns or high-explosive drivers. In Fig. 5, we show the state of knowledge before this work: experimental data were available to 90 GPa [46] and existing equation of state (EOS) models (SESAME 5181 and LEOS 360) exhibited markedly different behavior over this narrow range of compression. In this section, we compare the new experimental data and results from DFT/QMD simulation. The previous and newly developed tabular EOS models are compared to both sets of results over the entire pressure range along the Hugoniot.

A. Shock Hugoniot of liquid krypton

Figures 6 and 7 compare the Z experimental data, the tabular EOS models, and the DFT results using the improved PAW and 18-electron PAW described earlier. In the U_S-U_P plane, the DFT and experimental data are in good agreement. The LEOS Y360 table reproduces both data sets up through the highest 18-electron PAW DFT data point. The weighted linear fit to the experimental data is

$$U_S = (1.313 \pm 0.225) + (1.231 \pm 0.017)U_P \qquad (1)$$

and is valid for $U_P > 9$ km/s. The off-diagonal covariance term for the fit is $\sigma_{C_0}\sigma_{S_1} = -3.834 \times 10^{-3}$.

The differences between the experimental, DFT, and tabular EOS models are more pronounced in the ρ-P plane, plotted in Fig. 7. At higher pressures, the experimental data show scatter that is likely caused by not directly measuring the flyer plate velocity. However, the experimental and DFT results show that previous EOS models (SESAME 5181 and LEOS

TABLE III. Experimental data for the reshock state in liquid krypton with an initial density of 2.43 g/cm^3.

Shot	Kr U_S (km/s)	Quartz U_S (km/s)	Kr ρ (g/cm^3)	Kr pressure (GPa)
Z2114	13.96 ± 0.04	16.86 ± 0.03	9.996 ± 0.261	423.4 ± 1.8
Z2294-N	15.01 ± 0.03	17.94 ± 0.04	10.270 ± 0.264	488.2 ± 2.5
Z2294-S	15.95 ± 0.05	18.93 ± 0.05	10.406 ± 0.284	552.2 ± 3.4
Z2148	17.82 ± 0.05	20.92 ± 0.04	10.530 ± 0.231	694.7 ± 3.1
Z2165	19.98 ± 0.04	23.14 ± 0.05	10.692 ± 0.201	876.0 ± 4.4
Z2196	20.68 ± 0.05	23.68 ± 0.05	11.039 ± 0.256	923.7 ± 4.5
Z2166	21.41 ± 0.09	24.16 ± 0.07	11.756 ± 0.549	967.2 ± 6.5

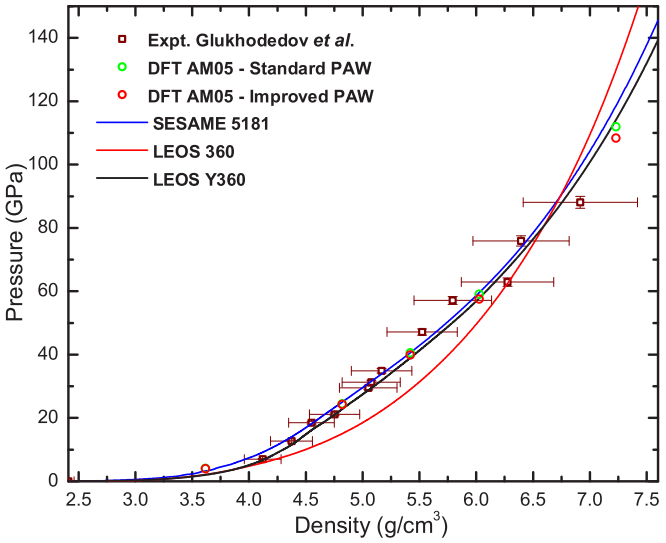

FIG. 5. (Color online) Shock Hugoniot of liquid krypton below 150 GPa. Both the standard and improved PAWs show good agreement with the experimental data from Ref. [46]. Th EOS tables are plotted for comparison.

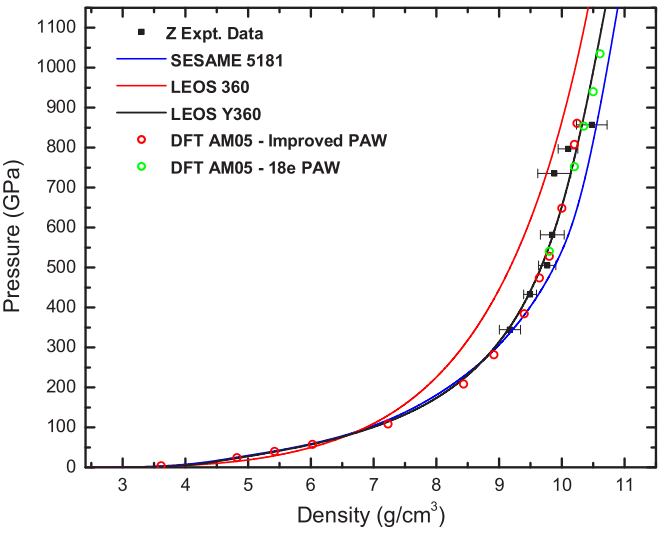

FIG. 7. (Color online) Shock Hugoniot of liquid krypton in the ρ-P plane showing good agreement between the DFT calculations and experimental data while highlighting differences with existing models.

360) do not describe the krypton Hugoniot at high pressures. Similarly to the liquid xenon Hugoniot [20], the previous EOS models bracket the true Hugoniot behavior likely because of their different treatments of the electronic component to the Helmholtz free energy. The LEOS Y360 table developed by Sterne [47] utilized the DFT and experimental principal Hugoniot results in its construction, thus reproducing the data.

B. Reshock state in krypton

In the experiment, the Kr shock velocity (U_S) is continuously measured as the shock transits the Kr sample. At higher flyer velocities, some attenuation of the shock velocity in the Kr can occur because of release waves produced from the melted portion of the flyer. Using the linear fit to the Z experimental data [Eq. (1)] and the measured U_S, we determine the Kr pressure, density, and particle velocity prior to the shock reflecting from the Kr/quartz interface. The particle velocity and pressure in the reshock state are accurately known because they are determined from the quartz standard [45]. The Rankine-Hugoniot equations are solved to determine the Kr density in the second shock state. Table III lists the experimental observables (Kr U_S and quartz U_S) and the calculated final density and pressure state in the Kr. Figure 8 shows the Kr reshock data compared to the reshock states determined using the LEOS Y360 table. Reshock paths are calculated using the Y360 table and impedance matching to the quartz Hugoniot to determine the reshock envelope of states. The Y360 EOS shows good agreement over the examined pressure range, a sign that the EOS table is valid along the principal Hugoniot and also for off Hugoniot states reached via repeated shocks.

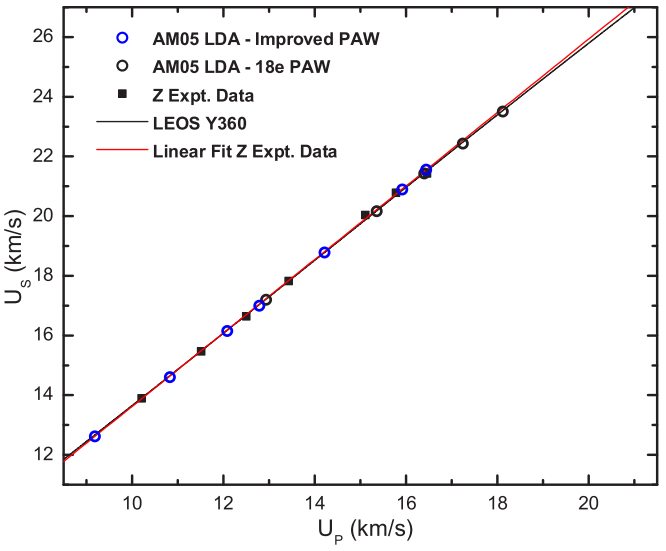

FIG. 6. (Color online) Shock Hugoniot of liquid Kr in the U_S-U_P plane. The behavior is linear and the DFT calculations show good agreement with the experimental data. The Y360 EOS reproduces the data.

C. Shock temperature of liquid krypton

The temperature of shocked material is of great importance, but subject to significant uncertainties due to lack of experimental data. Results from QMD simulations are often the only temperature information available. It is therefore of importance to compare QMD based estimations of temperature of shock states with EOS tables/models. Figure 9 plots the Hugoniot temperature calculated using the Y360 EOS table and the DFT temperatures. The EOS model and DFT temperatures show good agreement over the examined pressure range better than 5% for pressures below 1000 GPa. The agreement suggests that the thermal models used in design of Y360 are appropriate for this pressure range.

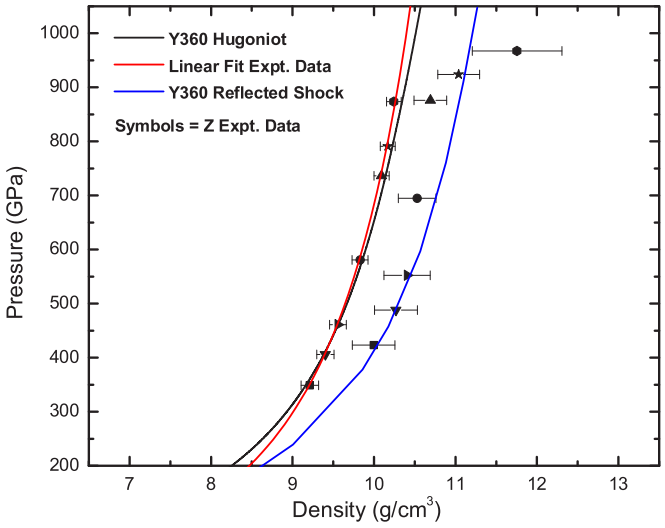

FIG. 8. (Color online) The experimental reshock data and calculated reshock envelope using the LEOS Y360 EOS table and quartz Hugoniot [45]. The different symbols connect measurements from the same experiment, for instance, the shock state marked by the square at ≈345 GPa and 9.2 g/cc was the intial state for the reshock measurement also marked by a square at ≈423 GPa and 10.0 g/cc. The reshock state probes compression at higher density (lower temperature) than the corresponding first shock state. Again, the LEOS Y360 table performs well, capturing the reshock states.

D. Equation of state models

The difficulty in describing high energy-density materials at several Mbar without the use of first-principles simulations like QMD is evident from the behavior of the different models shown in Figs. 5 and 7. Traditionally, EOS models are calibrated Hugoniot data from plate impact experiments and isothermal data from diamond anvil cells (DAC). Extrapolation beyond the range of experiments is challenging. Most expressions for the free energy of a material utilize a separation between contributions from cold compression (the cold curve), thermal excitations of ions (ionic thermal model), and finally the contribution of thermal excitations of electrons (electronic thermal model). The problem is underconstrained in terms of experimental data, especially the thermal terms due to the lack of high-precision temperature measurements at high-pressure conditions. The resulting EOS is based on a separation of terms in the free energy that is not unique. While the combined behavior in pressure and energy leading to the Hugoniot condition is constrained by experiments, the behavior of different terms with pressure and temperature is not, often resulting in strong deviations between different EOS models as they are extrapolated to pressures of hundreds of GPa.

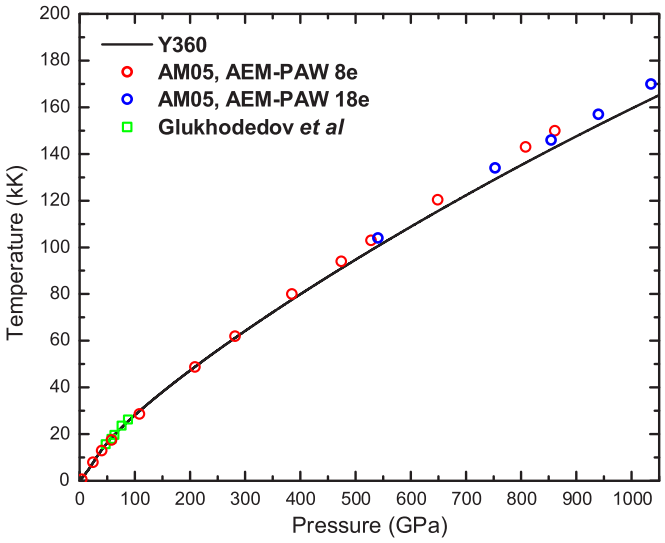

FIG. 9. (Color online) Temperature along the Hugoniot for liquid krypton: experimental data [46], DFT/QMD results, and calculated from the Y360 tabular EOS. The difference between DFT/QMD and Y360 increases with pressure although it remains smaller than 5% also at 1000 GPa/160 kK.

In the case of Kr, we find that the Y360 table reproduces the principal Hugoniot data over a wide range and also captures off-Hugoniot data as shown in Fig. 8. The Y360 table temperatures are also consistent with the QMD results over a wide range and thus we find that Y360 should be the preferred equation of state for Kr under high energy-density conditions.

V. SUMMARY

We have performed an extensive study of shock compressed liquid krypton up to 850 GPa on first shock and 950 GPa on reshock. Integration of DFT calculations and shock experiments provides a solid basis for understanding the behavior of krypton at extreme conditions. We demonstrate that QMD simulations can be performed with high precision also at temperatures above 10 eV (110 kK) provided that the high-energy scattering properties of the pseudopotentials/core potentials are verified. Furthermore, we find that the exchange-correlation functional AM05 captures the energetic variations in a cryogenic krypton liquid as calculated with quantum Monte Carlo, making it a good choice for krypton. The use of high-fidelity first-principles simulations allows for a significantly more detailed understanding of the different components of the free energy. QMD straightforwardly yields internal energy, pressure, structure, diffusion, and the entropy for solids. Recently, a method was developed that yields entropy [48] with very high precision, making QMD a complete method for first-principles thermodynamics. Successful application of QMD to thermodynamics, however, relies on performing converged simulations, using core potentials of high fidelity for high-temperature applications, and informed choices of exchange-correlation functionals.

ACKNOWLEDGMENTS

The authors thank all members of the Sandia Z facility that contributed to the design, fabrication, and fielding of the Z experiments. The authors especially appreciate the dedicated efforts of the cryo-team: A. Lopez, J. Lynch, J. Villalva, and K. Shelton as well as the engineering designs by D. Dalton and the diagnostics by C. Meyer. The work was supported by the NNSA Science Campaigns. L.S. was supported through the Predictive Theory and Modeling for Materials and Chemical Science program by the Office of

Basic Energy Sciences (BES), Department of Energy (DOE). Sandia National Laboratories is a multiprogram laboratory operated by Sandia Corporation, a wholly owned subsidiary of Lockheed Martin Company, for the U. S. Department of Energy's National Nuclear Security Administration under Contract No. DE-AC04-94AL85000.

APPENDIX: PAW CONSTRUCTION AND VALIDATION

In practice, when performing DFT calculations of warm dense matter, chemically inert core electrons are replaced by a pseudopotential (PP) and only the valence electrons are treated explicitly. High-quality PPs are available for VASP [28] and other codes. The quality is usually determined by comparing zero-temperature lattice constants and bulk moduli with results from equivalent calculations with an all-electron code. It is important to note that the quality of a PP can only be determined by comparison to all-electron calculations and never by comparison to experiment. The key issue is ensuring their transferability. A PP is usually constructed from the all-electron results of a single, free, spherically symmetric atom. For this atom, the PP generally produces the same results as an all-electron calculation. However, the success of transferring a PP to a different environment, such as to an atom in a bulk lattice, is dependent on a number of factors. Until recently, most PPs have been constructed for bulk matter at equilibrium and at fairly low temperatures. We use the projector augmented wave (PAW) PPs distributed with VASP. We note that while this investigation was made in the context of the PAWs used in VASP, the concepts are general to any DFT code that uses pseudopotentials. While these PPs usually produce very good zero-temperature equilibrium lattice constants and bulk moduli, the accuracy may not hold for high energy-density applications. The use of these PAWs constructed for low temperatures in extreme environments can produce less reliable results, as evident both in this work and in previous work on xenon [30].

Additional considerations needed for using PPs at high temperature and pressure are illustrated in Fig. 10. In Fig. 10, we plot the arc tangent of the logarithmic derivative at R,

$$\left.\frac{d\ln\phi(r)}{dr}\right|_{r=R} = \left.\frac{d\phi(r)}{dr}\right/\left.\phi(r)\right|_{r=R}, \tag{A1}$$

of radial wave functions of different angular momentum versus the energy of the wave function, calculated in the krypton atom with the PAW potential (colored dotted lines) compared to the all-electron results (black/gray dotted lines). Fermions (electrons) occupy states around the Fermi energy according to the temperature-dependent Fermi-Dirac distribution. As seen in Fig. 10, the distribution at high temperature (black full line, 180 000 K) is considerably wider than at room temperature (gray dashed line). The quality of the wave functions above the Fermi energy thus needs to be much higher at larger temperatures. It is clear that the standard PAW potential in Fig. 10(a) is not suitable for larger temperatures while being adequate for low temperatures.

We constructed [49] a new PAW potential for krypton from the same 8 valence electron atomic configuration as the standard potential, using the f atomic orbital for the local potential instead of the d, decreasing the partial core radius from 2.00 to 1.80 bohrs, and adding projectors to both the p and d channels. The pertinent information for the projectors is summarized by a giving the energy and the cutoff radius from the description field in the VASP POTCAR

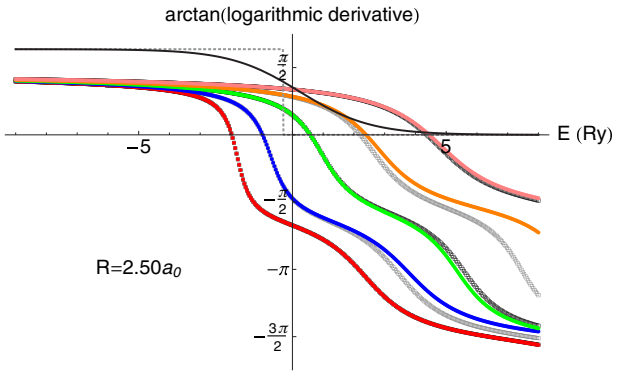

(a) Standard (8 electron) Kr PAW (PAW Kr 07Sep2000)

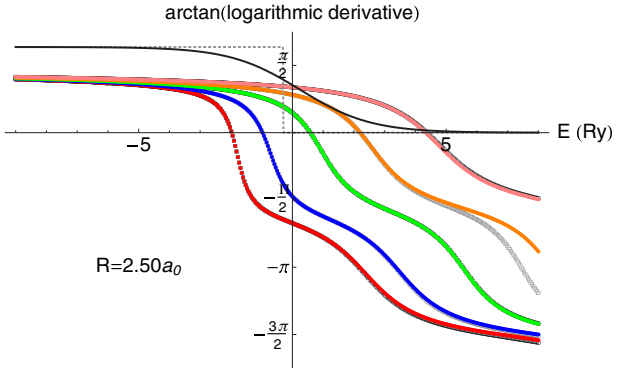

(b) New 8 electron Kr PAW

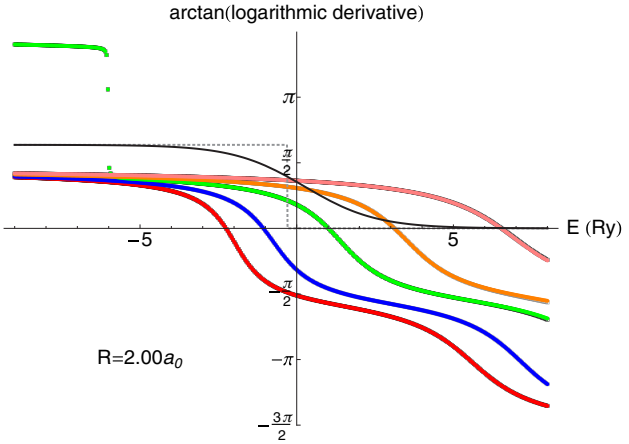

(c) New 18 electron Kr PAW

FIG. 10. (Color online) Logarithmic derivatives of atomic radial wave functions at distance R from the nucleus as a function of energy. Colored lines are s (red), p (blue), d (green), f (orange), and g (pink) angular momentum solutions from a pseudopotential calculation. They are compared to the corresponding black/gray all-electron solutions. The black full (gray dashed) line shows the Fermi-Dirac distribution at 180 000 K (300 K) with the Fermi energy that of an isolated atom.

file:

```
Description
  l          E          RCUT
  0     −23.1713547     1.800
  0     −16.3269912     1.800
  1      −9.3927349     2.000
  1       1.3605826     2.000
  2      −1.3605826     2.300
  2      27.2116520     2.300
  3      −1.3605826     2.300,
```

where l is the angular momentum of the given projector, cutoff distances (RCUT) are in bohrs, and projector energies (E) in eV. This results in the PAW potential with the same outmost cutoff radius of 2.30 bohrs and a slightly larger recommended kinetic energy cutoff (ENMAX 239.322 versus 185.392 eV), used in Fig. 10(b). Comparing Figs. 10(a) and 10(b), an improvement is evident, particularly in the p and f channels. This PAW potential is adequate for considerably higher temperatures compared to the standard PAW potential used in Fig. 10(a).

While the new Kr PAW potential might be adequate for the temperatures reached in our calculations, the very high-pressure conditions need to be taken into account as well. It is important to consider if the inert core approximation is valid at these higher temperatures and pressures. A concern was that the lowest valence electron energy levels in the calculations were not fully occupied in our calculations. That is, the Fermi-Dirac distribution at these high temperatures also affected the lowest-energy electrons explicitly included in the calculations. Depending on the electronic structure, this may be a sign of including too few valence electrons. In addition, when investigating the average particle distance, we found that a substantial fraction of the electrons were closer than two times the outmost core radius of the potential [49]. Again, overlap does not automatically disqualify a potential, but these two occurrences suggest that the electrons in the highest-lying core levels are not inert and we need to add them to the valence in order to treat them explicitly and reduce the core radii.

In Fig. 10(c) we show the results at the smaller R of 2.0 bohrs, from the new PAW potential where the 10 d electrons are added to the valence. The partial-core radius is decreased further to 1.40 bohrs, and all cutoff radii are reduced and projectors added:

```
Description
  l          E          RCUT
  0     − 23.1713547     1.500
  0     − 9.5240782      1.500
  0      129.2553470     1.600
  1     − 9.3927349      1.700
  1     − 4.0817478      1.700
  1      102.0436950     1.900
  2     − 81.7651686     1.500
  2     − 1.3605826      1.500
  2      27.2116520      1.600
  3     − 1.3605826      1.600.
```

The resulting plane-wave cutoff energy ENMAX is almost tripled; 680.776 eV, and the outmost core radius reduced to 1.90 bohrs, a value more commensurate with the high densities in our calculations. As seen in Fig. 10(c), the logarithmic derivatives are improved considerably even at this smaller distance from the nucleus, and this PAW potential should be adequate for all calculations presented here. Note that the Fermi-Dirac distribution for very large temperatures, in fact, reaches down to the distinct step feature at ~ -6 Ry (-81.76 eV) marking the very narrow band of $3d$ (core) levels. However, with this potential, more of the electrons need to be explicitly treated in the calculations and it also requires a higher kinetic energy cutoff, making it more computationally expensive.

Good agreement between the logarithmic derivatives of the wave functions in PP and all-electron calculations on an atom is a necessary but not sufficient condition of appropriateness. Further testing should be considered, such as the usual calculations of equilibrium properties of a solid. For our applications, it is also valuable to compare density of states for some relevant atomic configurations calculated with the PP and compared to an all-electron calculation [49], in particular to identify ghost states at high energies.

[1] P. Hohenberg and W. Kohn, Phys. Rev. **136**, B864 (1964); W. Kohn and L. J. Sham, *ibid.* **140**, A1133 (1965).

[2] M. P. Desjarlais, Phys. Rev. B **68**, 064204 (2003).

[3] M. D. Knudson, M. P. Desjarlais, and D. H. Dolan, Science **322**, 1822 (2008).

[4] M. D. Knudson and M. P. Desjarlais, Phys. Rev. Lett. **103**, 225501 (2009).

[5] M. D. Knudson, M. P. Desjarlais, R. W. Lemke, T. R. Mattsson, M. French, N. Nettelmann, and R. Redmer, Phys. Rev. Lett. **108**, 091102 (2012).

[6] S. Root, K. R. Cochrane, J. H. Carpenter, and T. R. Mattsson, Phys. Rev. B **87**, 224102 (2013).

[7] N. Mermin, Phys. Rev. **137**, A1441 (1965).

[8] T. R. Mattsson, J. M. D. Lane, K. R. Cochrane, M. P. Desjarlais, A. P. Thompson, F. Pierce, and G. S. Grest, Phys. Rev. B **81**, 054103 (2010).

[9] R. Boehler, M. Ross, P. Söderlind, and D. B. Boercker, Phys. Rev. Lett. **86**, 5731 (2001).

[10] D. Errandonea, B. Schwager, R. Boehler, and M. Ross, Phys. Rev. B **65**, 214110 (2002).

[11] I. V. Aleksandrov, A. N. Zisman, and S. M. Stishov, Zh. Eksp. Teor. Fiz. **92**, 657 (1987).

[12] A. Polian, J. M. Besson, M. Grimsditch, and W. A. Grosshans, Phys. Rev. B **39**, 1332 (1989).

[13] A. Polian, J. P. Itie, E. Dartyge, A. Fontaine, and G. Tourillon, Phys. Rev. B **39**, 3369 (1989).

[14] A. E. Mattsson, P. A. Schultz, M. P. Desjarlais, T. R. Mattsson, and K. Leung, Modell. Simul. Mater. Sci. Eng. **13**, R1 (2005).

[15] J. P. Perdew and A. Zunger, Phys. Rev. B **23**, 5048 (1981).

[16] R. Armiento and A. E. Mattsson, Phys. Rev. B **72**, 085108 (2005).

[17] W. Kohn and A. E. Mattsson, Phys. Rev. Lett. **81**, 3487 (1998).

[18] A. E. Mattsson, R. Armiento, J. Paier, G. Kresse, J. M. Wills, and T. R. Mattsson, J. Chem. Phys. **128**, 084714 (2008).
[19] P. Haas, F. Tran, and P. Blaha, Phys. Rev. B **79**, 085104 (2009).
[20] S. Root, R. J. Magyar, J. H. Carpenter, D. L. Hanson, and T. R. Mattsson, Phys. Rev. Lett. **105**, 085501 (2010).
[21] L. Shulenburger and T. R. Mattsson, Phys. Rev. B **88**, 245117 (2013).
[22] A. Benali, L. Shulenburger, N. A. Romero, J. Kim, and O. A. von Lilienfeld, J. Chem. Theory Comput. **10**, 3417 (2014).
[23] G. L. Pollack, Rev. Mod. Phys. **36**, 748 (1964).
[24] D. L. Losee and R. O. Simmons, Phys. Rev. **172**, 944 (1968).
[25] J. Kim, K. P. Esler, J. McMinis, M. A. Morales, B. K. Clark, L. Shulenburger, and D. M. Ceperley, J. Phys.: Conf. Ser. **402**, 012008 (2012).
[26] M. A. Morales, J. R. Gergely, J. McMinis, J. M. McMahon, J. Kim, and D. M. Ceperley, J. Chem. Theory Comput. **10**, 2355 (2014).
[27] R. C. Clay, J. Mcminis, J. M. McMahon, C. Pierleoni, D. M. Ceperley, and M. A. Morales, Phys. Rev. B **89**, 184106 (2014).
[28] P. E. Blöchl, Phys. Rev. B **50**, 17953 (1994); G. Kresse and D. Joubert, *ibid.* **59**, 1758 (1999).
[29] G. Kresse and J. Hafner, Phys. Rev. B **47**, 558(R) (1993); **49**, 14251 (1994); G. Kresse and J. Furthmüller, *ibid.* **54**, 11169 (1996).
[30] T. R. Mattsson and R. J. Magyar, in *Shock Compression of Condensed Matter – 2009*, AIP Conference Proceedings, Vol. 1195, edited by M. L. Elert *et al.* (AIP, Melville, New York, 2009), pp. 797–800.
[31] M. E. Savage, L. F. Bennett, D. E. Bliss, W. T. Clark, R. S. Coats, J. M. Elizondo, K. R. LeChien, H. C. Harjes, J. M. Lehr, J. E. Maenchen, D. H. McDaniel, M. F. Pasik, T. D. Pointon, A. C. Owen, D. B. Seidel, D. L. Smith, B. S. Stoltzfus, K. W. Struve, W. A. Stygar, L. K. Warne, J. R. Woodworth, C. W. Mendel, K. R. Prestwich, R. W. Shoup, D. L. Johnson, J. P. Corley, K. C. Hodge, T. C. Wagoner, and P. E. Wakeland, in 2007 IEEE Pulsed Power Conference, Vols. 1-4 (IEEE, New York, 2007), pp. 979–984.
[32] R. Lemke, M. Knudson, D. Bliss, K. Cochrane, J.-P. Davis, A. Giunta, H. Harjes, and S. Slutz, J. Appl. Phys. **98**, 073530 (2005).
[33] M. D. Knudson, J. R. Asay, and C. Deeney, J. Appl. Phys. **97**, 073514 (2005).
[34] S. Root, T. A. Haill, J. M. D. Lane, A. P. Thompson, G. S. Grest, D. G. Schroen, and T. R. Mattsson, J. Appl. Phys. **114**, 103502 (2013).
[35] D. Hanson, R. Johnson, M. Knudson, J. Asay, C. Hall, J. Bailey, and R. Hickman, in *Shock Compression of Condensed Matter–2001*, AIP Conference Proceedings, Vol. 620, edited by M. D. Furnish, N. N. Thadhani, and Y. Horie (AIP, Melville, New York, 2001), p. 1141.
[36] A. C. Hollis-Hallet, in *Argon, Helium, and the Rare Gases*, Vol. 1, edited by G. A. Cook (Interscience, New York, 1961), Chap. 9, p. 359.
[37] G. T. Clayton and L. Heaton, Phys. Rev. **121**, 649 (1961).
[38] M. J. Terry, J. T. Lynch, M. Bunclark, K. R. Mansell, and L. A. K. Staveley, J. Chem. Thermodyn. **1**, 413 (1969).
[39] C. Gladun and F. Menzel, Cryogenics **10**, 210 (1970).
[40] A. C. Sinnock and B. L. Smith, Phys. Rev. **181**, 1297 (1969).
[41] L. M. Barker and R. E. Hollenbach, J. Appl. Phys. **43**, 4669 (1972).
[42] D. H. Dolan, Sandia Technical Report No. SAND2006-1950, 2006 (unpublished).
[43] G. E. Duvall and R. A. Graham, Rev. Mod. Phys. **49**, 523 (1977).
[44] M. D. Knudson, R. Lemke, D. Hayes, C. A. Hall, C. Deeney, and J. Asay, J. Appl. Phys. **94**, 4420 (2003).
[45] M. D. Knudson and M. P. Desjarlais, Phys. Rev. B **88**, 184107 (2013).
[46] V. D. Glukhodedov, S. I. Kirshanov, T. S. Lebedeva, and M. A. Mochalov, J. Exp. Theor. Phys. **89**, 292 (1999).
[47] P. A. Sterne (private communication).
[48] M. P. Desjarlais, Phys. Rev. E **88**, 062145 (2013).
[49] A. E. Mattsson, Sandia Technical Report No. SAND2012-7389, 2012 (unpublished).